Proceedings of the ASME 2019 38th International Conference on Ocean, Offshore and Arctic Engineering
OMAE2019
June 9-14, 2019, Glasgow, Scotland

DRAFT

OMAE2019-96043

INVESTIGATION OF FOCUSED WAVE IMPACT ON FLOATING PLATFORM FOR OFFSHORE FLOATING WIND TURBINE – A CFD STUDY

Yang Zhou[1], Qing Xiao[1*], Yuanchuan Liu[1], Atilla Incecik[1]
Department of Naval Architecture, Ocean and Marine Engineering, University of Strathclyde
Glasgow, G4 0LZ, UK

Christophe Peyrard[2]
Saint-Venant Hydraulics Laboratory (Électricité de France, ENPC, Cerema), Université Paris-Est, 6 quai Watier, 78400 Chatou, France

ABSTRACT

Most existing research related to a semi-submersible offshore floating platform focuses on the wave-structure interaction under either a regular or irregular wave condition. In order to numerically model the irregular wave impact on a semi-submersible platform hydrodynamic response with a low computational cost, in this study, a focused wave is utilized. The platform under this consideration is the DeepCwind semi-submersible platform. A high fidelity CFD numerical solver based on solving Navier-Stokes equations is adopted to estimate the dynamic response and the hydrodynamic loading of the platform. The focused wave is firstly generated based on a first order irregular wave theory in a numerical wave tank and validated against the linear wave theory results. Next, for CFD coding validation, the surface elevation of a fixed FPSO model associated with a focused wave is calculated and compared with the benchmark results. At last, the dynamic responses of the platform are numerically simulated under various focused wave parameters, and the results are compared with those obtained from an in-house potential flow theory tool at Électricité de France (EDF). It is found that the predicted CFD surge motion responses are close to those achieved with the second order potential theory while differ from the results obtained using linear potential theory. As to the pitch motion, differences are observed between two results, due to the different methods used for second order loads and viscous effects calculation. Turning to the results under different wave parameters, the surge and heave motion responses increase as the wave period goes up. However, the pitch motion is not affected significantly by varying wave periods. It may be due to the fact that the low-frequency effects have limited impact on the pitch motion. The strong nonlinearity at extremely large wave amplitude will be the task in our near future study.

INTRODUCTION

As one of the clean and renewable energy, wind energy has raised the worldwide attention and experienced rapid growth in the past decade. According to the European Wind Energy Association reports in 2018, the wind energy takes account of nearly more than half of the new power generation in the last year [1]. Compared to the onshore wind power facilities and the bottom-fixed structures, offshore floating wind turbines (OFWT) will unlock the countless wind resource at distant and deeper sites. However, OFWT requires relatively higher installation, construction and maintenance expense due to the complicated operating conditions [2], especially the risk of the damage of floating platform and mooring system under some hush wave conditions. It is thus desirable to examine the interactions between a moored offshore structure and the incident wave, as the sustainability of such floating platforms is crucial to a whole OFWT system especially under unexpected extreme wave conditions.

Most research related to the hydrodynamic loading and motion response of the OFWT platform mainly focuses on either regular or irregular wave conditions. Tran and Kim [3] investigated a semi-submersible platform dynamic response and mooring tension by using a commercial CFD software STAR-CCM+, their results showed a good agreement with the data from the experiment and NREL FAST. Liu et al. [4] developed a fully coupled CFD numerical tool to simulate the complex fluid-structure interactions between wind/wave flows and the OFWT by using OpenFOAM. With a nonlinear computational model, Nematbakhsh et al. [5] studied a spar supported floating wind turbine in extreme sea states under irregular waves conditions. Strong nonlinear effects were captured in the surge, heave and pitch responses.

A focused wave is believed to be one of the extreme waves, in which a number of waves components add up at a specific time and space point. Because of these specific features, focused

[1] Contact author: qing.xiao@strath.ac.uk

wave study has been used as a cost-effective approach to examine the offshore structures dynamics under extreme wave conditions. Baldock et al. [6] designed a focused wave by the superposition of a group of regular wave trains. With that, they investigated the nonlinearity of wave-wave interaction of focused waves. Ning et al. [7] investigated the nonlinear effects on a semi-submerged horizontal cylinder column under focused waves. The results were compared with a regular wave having identical wave crest and trough-to-trough period. Generating a focused wave by using NewWave with a JONSWAP spectrum, Mai et al. [8] reported a wave tank test on a series of FPSO (floating production storage and off-loading). With the measured surface elevation and wave run-up data, their study shed insights on the interaction between a focused wave and a fixed offshore structure.

As a brief review in the above, it is noted that the previous focused wave studies are either limited to a fixed offshore structure or a simple floater like a cylinder column or a simplified ship model, less attention has been drawn to the floaters used for offshore floating wind turbine system. To bridge this gap, in this study, we will use a high-fidelity CFD numerical modelling tool to investigate the dynamic responses and the hydrodynamic loadings of a semi-submersible platform under the focused wave. The investigation will cover a couple of cases with different wave parameters. The CFD results will be compared with the results obtained from a potential theory tool from EDF to illustrate the viscous or non-linearity impact.

Numerical models

The incompressible Navier-Stokes(N-S) equations are solved for the viscous flow model while a volume of fluid (VOF) method is utilized for two-phase flow in order to capture the free surface. Finite volume method is adopted to solve the N-S equations. A wave generation utility [9] based on the multiphase solver "interFoam" in OpenFOAM [10] is incorporated to generate and absorb waves.

Governing equation

The continuity equations for a transient, incompressible and viscous fluid reads:

$$\nabla \cdot U = 0 \tag{1}$$

In addition, the Navier-Stokes equations are written as

$$\frac{\partial \rho U}{\partial t} + \nabla \cdot \left(\rho(U - U_g)U\right) = -\nabla P_d - g \cdot x \nabla \rho + \nabla\left(\mu_{eff} \nabla \mathrm{U}\right) + (\nabla \mathrm{U}) \cdot \mu_{eff} + f_\sigma \tag{2}$$

Where U and U_g refer to the velocity of flow field and grid nodes in Cartesian coordinates, ρ is the mixed density of water and air, g is the gravity acceleration. P_d represents the dynamic pressure instead of the total pressure. $\mu_{eff} = \rho(v + v_t)$ is the effective dynamic viscosity, in which v and v_t are the kinematic and eddy viscosity respectively. f_σ is the surface tension, which only take into consideration at the free surface.

Free surface capture

In order to capture the water-air free surface, the Volume of Fluid (VOF) method [11] is adopted, using the following transport equations to govern the volume fraction variable α,

$$\frac{\partial \alpha}{\alpha t} + \nabla \cdot \left[(U - U_g)\alpha\right] + \nabla \cdot [U_r(1 - \alpha)\alpha] = 0 \tag{3}$$

In order to assure the boundedness and conservativeness of the volume fraction α, a third compression term on the left-hand side of the transport equations is introduced, where U_r is a velocity field to compress the interface as the compression velocity. The last term on the left hand side is referred as the interface compression term, which only functions near the free surface due to the inclusion of $(1 - \alpha)\alpha$. For a multiphase flow problem, the volume fraction of each liquid is used as the weighting factor to get the mixture properties, for the density and the viscosity,

$$\rho = \alpha\rho_w + (1 - \alpha)\rho_a \tag{4}$$

$$\mu = \alpha\mu_w + (1 - \alpha)\mu_a \tag{5}$$

Where ρ_w and ρ_a are the density of water and air. Furthermore, μ_w and μ_a refer to the viscosity coefficient of water and air respectively.

Wave generation and absorbing

Toolbox "waves2Foam" [9] is used to generate and absorb free surface waves in a numerical wave tank. The relaxation zone technique is adopted to provide better wave quality and to avoid wave reflection in the absorbing zone, which are applied at the inlet and outlet boundaries of the numerical wave tank. The following equations specify the main function of the relaxation zones,

$$\alpha_R(\chi_R) = 1 - \frac{\exp({\chi_R}^{3.5}) - 1}{\exp(1) - 1} \tag{6}$$

$$\phi_R = \omega_R \phi_R^{computed} + (1 - \omega_R)\phi_R^{target} \tag{7}$$

Where the ϕ_R refers to either the velocity or volume fraction of water α. The definition of χ_R is that the weighting functions α_R is always 1 at the interface between the non-relaxed computational domain and the relaxation zones, and χ_R is a value between 0 and 1. The relations between χ_R and α_R are shown in Figure 1.

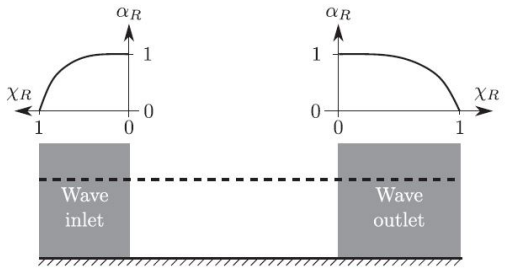

Figure 1 Diagrams of the variation of $\alpha_R(\chi_R)$ in relaxation zones (both inlet and outlet)

For the superscript *computed* and *target* represents the value calculated in the computational domain and evaluated from the chosen wave model respectively.

Focused wave generation

The focused wave is generated with the first order irregular wave theory, which is a linear superposition of individual regular wave components. The spectral shapes of irregular waves are implemented by the JONSWAP spectrum[12]. The significant wave height Hs, peak angular frequency ω_p and shape factor γ are the main input parameters to the JONSWAP spectrum,

$$S_j(\omega) = \frac{5}{16} H_s^2 \omega_p^5 \omega_j^{-5} (-\frac{5}{4}) \exp((\frac{\omega_j}{\omega_p})^{-4}) \gamma^r \quad (8)$$

Based on the irregular wave theory, modulation of phase angle among individual wave components can achieve a large amount of wave train energy at a fixed time spot. The wave peak superposition at a fixed time and position is mathematically represented as

$$\cos(k_i x - \omega_t + \tau_i) = 1 \quad (9)$$

Where k_i is the wave number and ω_t is the angular frequency of each regular wave component, τ_i is the phase angle of each regular wave. The phase angle of the wave component is written as

$$\tau_i = k_i x - \omega_t - 2\pi n, n = 0,1,2, \ldots \quad (10)$$

The wave elevation of the wave train at a focused position xc and a focused time tc is expressed as,

$$S(x,t) = \sum_{i=1}^{n} \frac{A_i}{2} * \cos(k_i(x - xc) + \omega_i(t - tc) \quad (11)$$

Mesh convergence and model validation of focused waves

Sensitivity study of numerical wave generation

In the present study, a 2D grid convergence test is firstly conducted for the focused wave generation. The numerical wave tank has the length of 24m (-12m<x<12m), the width of 1m (-0.5m<y<0.5m) and the height of 3m (-2m<z<1m). The water depth is set as 2m. The mesh convergence test is performed for a focused wave of significant wave height Hs=0.103m and the wave peak period Tp=1.456s. The focused position is set at x=0.0 m, while the focused time is set at 10s.

Three sets of mesh are used as listed in Table.1, which Hs refers to the significant wave height and L for the length of wave tank. The mesh number under testing are coarse mesh (17600), medium mesh (24000) and fine mesh (32000).

Table 1 Mesh configuration of 3 sets of mesh

Refinement	Coarse	Medium	Fine
X axis	Δx= L/200	Δx= L/250	Δx= L/300
Z axis	Δz= Hs/6	Δz= Hs/8	Δz= Hs/10

Figure 2 summarises the amplitude variation with time compared with the analytical solution from linear theory. As seen from the figure, the predicted surface elevation results are consistent for all three meshes, but they all underestimate the wave height. It may be due to the attenuation of the regular wave components when the wave passes by in the relaxation zone. Moreover, Table 2 shows the errors between different mesh method of the maximum wave height and trough-to-trough period of the focused wave.

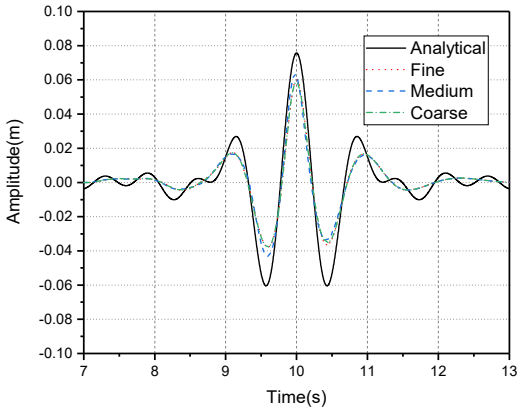

Figure 2 Surface elevation in time sequence from a numerical wave generation and an analytical solution

Table 2 Mesh sensitivity test under different mesh sizes

Grid	Coarse	Medium	Fine
Maximum wave height(m)	0.0991 (-0.60%)	0.1038 (+4.21%)	0.0996
Trough to trough period(s)	0.831 (+0.34%)	0.826 (-0.16%)	0.827

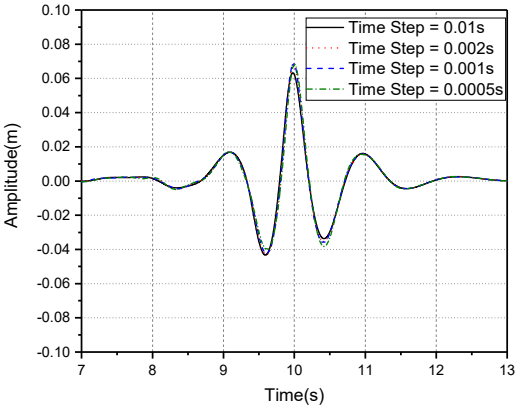

Figure 3 Surface elevation at the focused position with different time steps

Table 3 Mesh sensitivity test under different time steps

Time Step	0.01s	0.002s	0.001s	0.0005s
Maximum wave height(m)	0.1038 (-5.03%)	0.1106 (+1.19%)	0.1114 (+1.92%)	0.1093
Trough to Trough period(s)	0.826 (-1.38%)	0.836 (-0.15%)	0.836 (-0.15%)	0.837

The study of time step influence on the wave generation is performed with Δt = 0.01s, 0.002s, 0.001s and 0.0005s. The results in Figure 3 and Table 3 indicate no significant difference for the above various time steps.

Taking the computational time into consideration, the medium size of mesh is utilized for the following simulations.

Validation of a fixed FPSO and focused wave

The numerical verification for a focused wave-structure interaction problem is performed with a FPSO structure. The numerical results are compared with the wave tank data[8] operated in the Ocean Basin at Plymouth University's COAST Laboratory and other CFD results[13].

In this case, the significant wave height is given as 0.103 m, and the wave peak period goes to 1.456 s. The FPSO model is set at the waves focused position. The length, width and the depth of the numerical wave tank are 16m (-8m, 8m), 5m (-2.5m, 2.5m) and 5m (-3m, 2m) respectively. The total mesh is 442490, they are refined near the free surface and around the FPSO model.

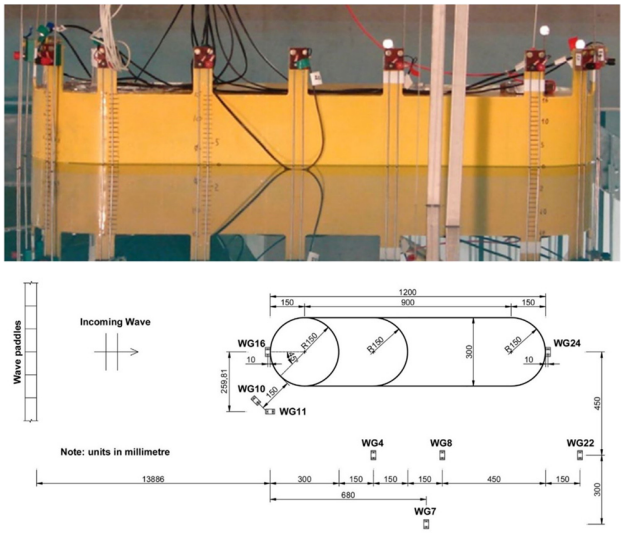

Figure 4 Layout of the test FPSO model

In Figure 5, the surface elevation data of WG16(x=0.0m) is plotted to compare with other CFD[13] and experimental results. As seen, the present CFD predicted results are comparable to the wave tank data and other CFD results. The surface elevation after 50 seconds differs with other results.

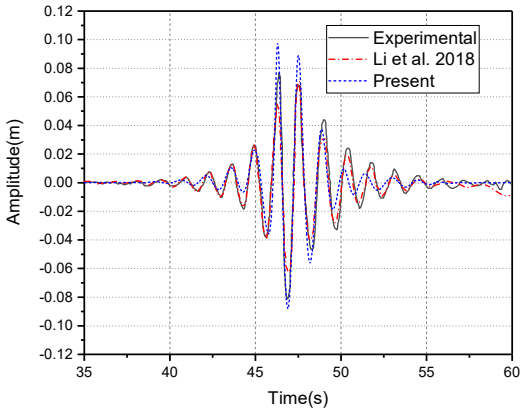

Figure 5 Free surface elevation at WG16

One possible explanation is that, during the focused wave generation, a range of frequencies in the spectrum must be specified to generate waves. The difference may be caused by different frequency range to generate the focused wave in the same spectrum. Another reason may result from the error waves produced after 50 seconds in the present simulation.

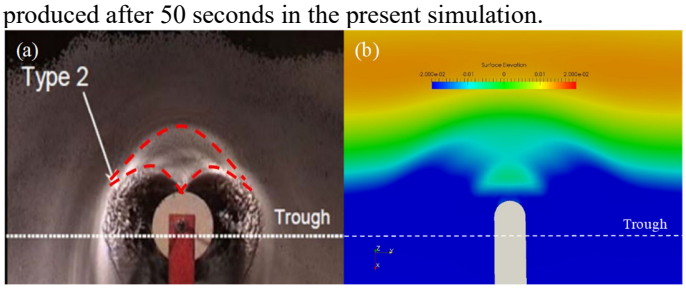

Figure 6 Free surface elevation around FPSO model (a) Wave tank test at t=50.7s (b) Present simulation at t=51s

The local instantaneous free surface elevation is captured and displayed in Figure 6, by comparing with the experimental results. Clearly, the CFD predicted flow field around FPSO is in a good agreement with the experimental data.

Model description of the floating platform

The floating platform investigated in this study is a semi-submersible floater, which has been widely examined as a floating platform to support offshore floating wind turbine in the project of OC4[14]. The floater consists of three columns with a relatively large diameter base, one middle column for supporting wind turbine and a series of crossing bracings to connect outer columns and inner one[15], as shown in Figure 7.

Gross properties of the platform and the mooring properties are listed in Table 4. The mass and the inertia of the platform include the wind turbine. Thus, the gross properties are slightly different from the wave tank data. For the present model, the

resonance period of the surge, heave and pitch goes to 107.0s, 17.5s and 26.8s.

Figure 7 Image of 1/50 scale DeepCwind semi-submersible platform model in MARIN tank

Table 4 Gross properties of semi-submersible platform including the mooring system

Platform gross properties		
	MARIN	Present
Platform mass, including ballast	13444000kg	14143400kg
Displacement	13986.8m^3	13986.8m^3
Centre of mass location below SWL along centre line	14.4m	10.2m
Platform pitch inertia about centre of mass	8.011×10^{9}kgm^2	1.317×10^{10}kgm^2
Platform yaw inertia about centre of mass	1.391×10^{9}kgm^2	1.906×10^{10}kgm^2
Platform roll inertia about centre of mass	8.011×10^{9}kgm^2	1.315×10^{10}kgm^2
Mooring line properties		
Number of mooring lines	3	
Angle between adjacent lines	120°	
Depth of anchors below SWL(water depth)	200m	
Upstretched mooring line length	835.5m	
Radius to anchors from platform centreline	837.6m	
Mooring line diameter	0.0766m	

CFD Model

Numerical method

In the present study, flow equations are solved by using the open source software OpenFOAM [10]. PISO (Pressure implicit with Splitting of Operator) algorithm is utilized to solve the pressure-velocity coupling. The largest allowed courant number (CFL) is set to 1. The time step is fixed as small as 0.002s. A first-order Euler scheme is used for time derivatives. The convective terms are approximated by second-order upwind scheme. Laminar model is used as indicated by Finnegan et al. [16] findings that there is no obvious disparity in simulating waves by using turbulence model and laminar model

Computational domain and boundary conditions

The sketch of the numerical model is shown in Figure 8. The computational domain extends in three dimensions, i.e. $-5D < x < 10D$, $-5D < y < 5D$ and $-4D < z < 3D$, which D is the distance between the adjacent outer columns of the floating platform. The water depth is 200m.

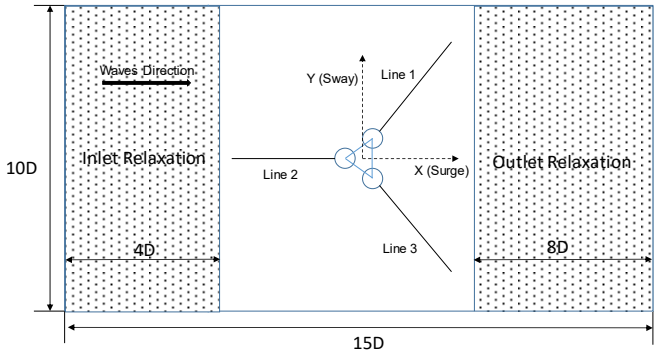

Figure 8 Sketch of the numerical simulation

The floating platform is located at the origin of the coordinate system to reduce the influence of the numerical boundaries. The length of the inlet and outlet relaxation zones are 4D and 8D respectively in order to provide a better wave quality and minimize the wave reflection of the outlet boundary.

To cope with the motion of the platform, the arbitrary mesh interface (AMI) method is adopted. Only three degrees of freedom (DoF) of the structure are numerically modelled, i.e. the surge, heave and pitch. In Figure 9, the overall computational domain is split into two cell zones. As the platform is in a dynamic status, the outer zone only translates surge and heave motions, while the inner zone experiences all 3 DoF motion.

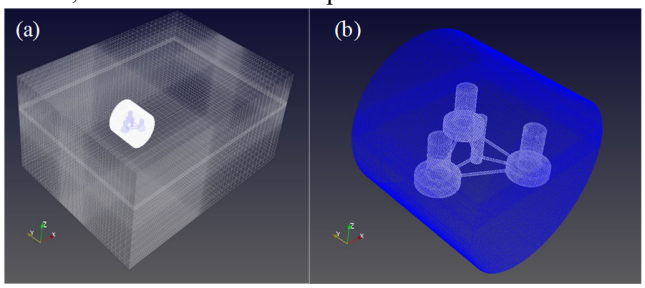

Figure 9 Computational mesh of semi-submersible floating platform (a) entire computational domain (b) AMI zone

The boundary conditions are defined as follows. At the inlet boundary (left side of inlet relaxation zone), the velocity is prescribed as the incident focused wave and the pressure gradient is set as zero. Moreover, the velocity is fixed as zero and the pressure has a zero gradient at the outlet boundary (right side of the outlet relaxation zone). The boundary condition of the upper part is set as atmosphere while the front and back boundary is referred to symmetry plane. The non-slip wall boundary condition with zero pressure gradient is defined on the surfaces of the semi-submersible platform.

The overall mesh is generated by utilizing a built-in tool snappyHexMesh in OpenFOAM. Mesh refinement is applied near the free surface, inner cell zones and the platform. The total mesh size is 2353906, it takes about 80 hours to achieve 200s time sequence results using 360 CPU cores.

A quasi-static mooring method is used for the mooring.

The verification study on the hydrodynamic performance of the same semi-submersible floating platform as the present one was successfully performed in our published paper [4].

Potential theory (EDF)

The industrial results based on a potential flow theory presented in this paper have been obtained using EDF R&D floating wind turbine aero-hydro-elastic solver CALHYPSO [17]. In this paper, only the hydrodynamic part of the code is used. The floater is regarded as rigid, only the 6 rigid body motions are solved in the time domain, using a Newmark time marching scheme. For the present paper, mooring lines are regarded as quasi-static and the catenary equation is used to capture their response to floater motion. As shown in [18], this assumption is not expected to influence the motions of the floater but only the tension level in lines, which are not studied in the paper. The hydrodynamic loads are computed in the frequency domain using the potential flow solver NEMOH, developed by Ecole Centrale de Nantes [19], which solves the diffraction and radiation problems. Then the Cummins approach [20] is applied for the time domain resolution. The convolution integral is used to account for radiation effects with a time window of 60s, which is enough regarding the typical RIRF of the floater. Two potential flow results are presented in this paper for comparison with CFD results : "first order" and "second order" potential flow. In the "second order model", forces are computed up to second order (QTF), and are applied in the time domain without bandwidth limitation. Even if not presented, it has been verified that the sum-frequency QTF have almost no influence on the floater motions, thus only difference-frequency loads are included in the present "second order" model. This result was expected for semi-submersibles. For the "first order model", only first order forces are applied with no consideration about floater motions. For both models, the viscous part of the hydrodynamic force is accounted for using strip theory on all columns and bracings, with homogeneous drag coefficient Cd=1. Sensitivity study have been performed on this value, but the motions have shown little variations when using Cd=0.6 or Cd=2. The tanks also experience viscous forces in the vertical direction, and a drag coefficient Cd = 5 has been used for forces in line with the tank neutral axis. The same formulation is considered for the central column with Cd=4. Regarding the wave theory, first order Stokes waves (Airy theory) have been used to compute the focused wave free surface elevation. A FFT is applied on the 200s long free surface elevation time series obtained with the CFD solver at a reference point (center of floater at t=0) in order to get the wave components of the focused wave. About 200 significant wave components are extracted for the cases considered here. Amplitudes and phases are then applied as imposed spectrum into CALHYPSO and it is verified that the free surface elevation is consistent with the inputs. Finally, the modified-Wheeler stretching model is applied to compute the undisturbed wave kinematics in the fluid domain. It is noted that wave kinematics are only used for viscous forces, as all other forces are included in the hydrodynamic database computed by NEMOH. The EDF CPU time is 40s for the 200s calculations performed in this study.

Results and discussions

Simulation cases

In the present simulation, the focused time of all cases is set at 70 s due to the limitation of the maximum phase lag of a single regular wave component (see τ_i in Equation 10). It is also a waste of computational cost if the focused time is set at a higher value. The focused position is set at the origin of the coordinates system, where the centreline of the DeepCwind semi-submersible platform locates.

Seven cases are simulated with one of the wave conditions (Case 3) being taken from Reference [21], where the OC4 5MW semi-submersible platform under irregular waves was studied. The rest of other cases are set with different wave periods and amplitudes with the reference data in North Sea.

Since the focused waves are generated by a JONSWAP spectrum with the parameters of significant wave height Hs and wave peak period Tp, these two parameters are indicated in Table 5 and Table 6 along with the maximum wave height H_{max} and wave period T_{Hmax} (trough-to-trough period of focused wave), which are post-processed from the time domain surface elevation results.

Table 5 Focused wave parameters with different T_{Hmax}

Case	1	2	3	4	5
Hs(m)	5.49	5.49	5.49	5.49	5.49
Tp(s)	9.3	10.3	11.3	12.3	13.3
H_{max}(m)	5.651	6.463	6.613	6.541	6.464
T_{Hmax}(s)	8.0	8.40	8.75	9.25	9.5

Table 6 Focused wave parameters with different H_{max}

Case	3	6	7
Hs(m)	5.49	4.49	6.49
Tp(s)	11.3	11.3	11.3
H_{max}(m)	6.613	5.463	7.715
T_{Hmax}(s)	8.75	8.75	8.75

Figure 10 shows the surface elevation for all seven cases without the platform. In general, they are very similar, displaying a trend of an increased surface elevation as the wave peak period and significant wave height increases.

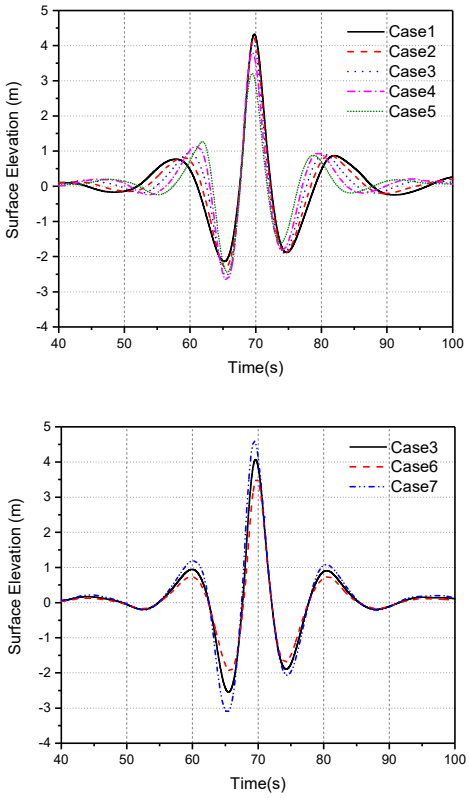

Figure 10 Surface elevation of sea states with different T_{Hmax} & H_{max}

Platform hydrodynamic responses under focused wave

The floating platform hydrodynamic responses are then simulated for the cases in Table 5 and Table 6. The dynamic response data is compared with the potential flow results provided by EDF. Since the differences between the two sets of results are similar for all seven cases, a full detailed discussion will be focused on Cases 3 only.

The free surface variation around the platform from t = 64 s to t = 74 s is shown in Figure 11 for Case 3.

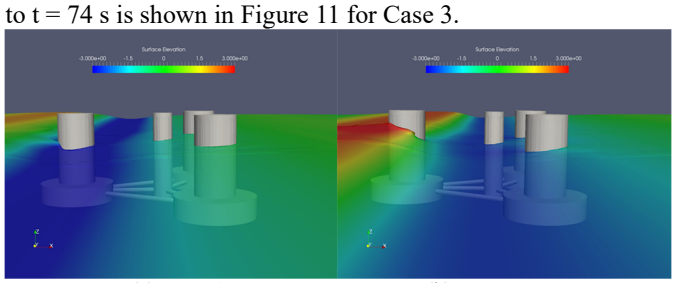

(a) T = 64.0s (b) T = 66.0s

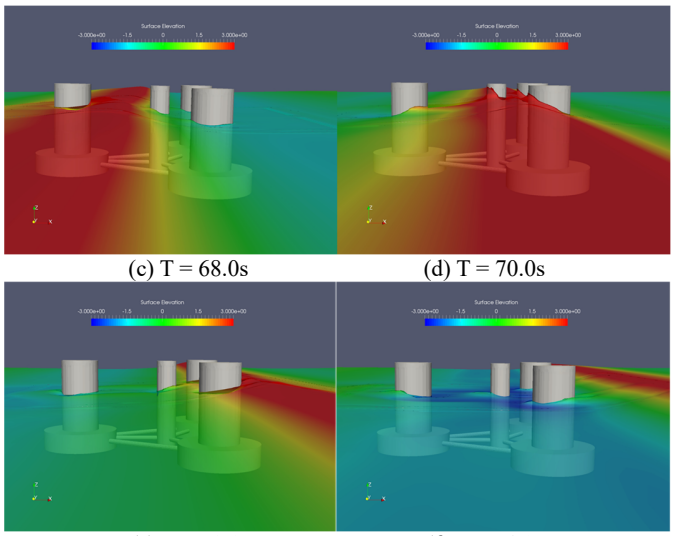

(c) T = 68.0s (d) T = 70.0s

(e) T = 72.0s (f) T = 74.0s

Figure 11 Free surface elevation around platform for Case 3 (H_{max} =6.613m T_{Hmax}= 8.75s)

As seen, the incident waves propagate along the positive x direction, with a focused wave reaching at the centreline of the platform. At that point, the wave run up is extremely large for the centre column, higher than other outer columns,

The hydrodynamic motions of the floating platform are compared with the potential flow results provided by EDF in all 7 cases. The results between CFD, linear results and second order results are quite similar in each simulation. For a better understanding, the results comparison of Case 3 is given in Figure 12.

The time series for surge and pitch motion are displayed in Figure 12 along with the results from the linear potential theory and a second order potential theory from EDF. The platform motions are induced by the incident focused wave before 100 s. An obvious secondary cycle can be observed around 95 s mainly due to the wave -structure interaction. After 100 s, the platform motions present a free decay trend.

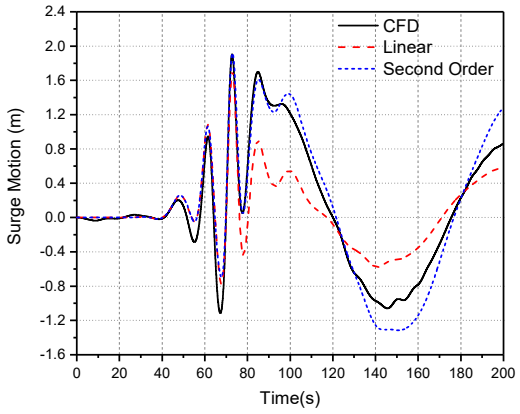

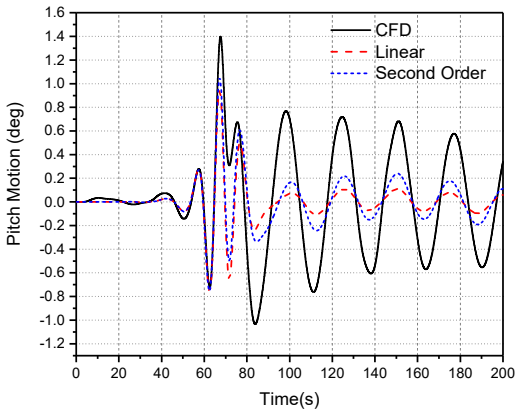

Figure 12 Surge and Pitch motion in time domain of Case3 (linear and second order results are obtained from EDF code)

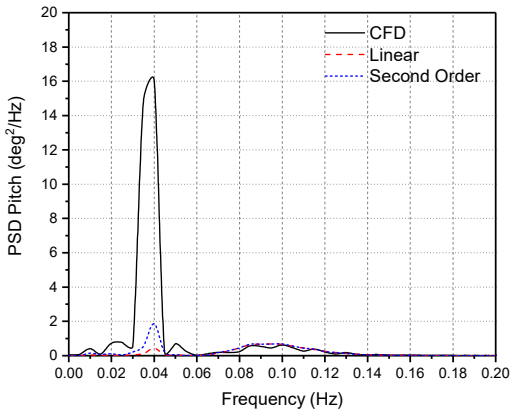

Figure 13 Comparisons of PSDs between CFD and Potential theory for Case3

For the surge motions comparison, before the focused time at 70 s, the platform response is captured commendably from all three results. The largest response of the platform occurred around 72 s. However, moving into the response after focused time, the CFD results compared well with the one based on the second order theory. The response of linear theory has a rather small amplitude. The neglecting of the mean drift force associated with the linear theory may be the reason, which leads to such a disparity. Turning to the pitch motion, CFD results are close to EDF one before 70s, but show some differences after the focused time. In particular, potential flow approach predicts lower ultimate pitch response (1°) than the CFD model (1.4°). One potential reason could be due to the fact that, CFD modelling takes into account the viscous force in a more accurate way than EDF model, which uses the potential flow approach. To account for the viscous effects, a drag coefficient and a Morison-like formulation of the drag force, based on incoming wave kinematics is included. Such viscous impact should become more significant when the hydrodynamic nonlinearly occurs, in particular considering the incoming wave field perturbation due to the floater.

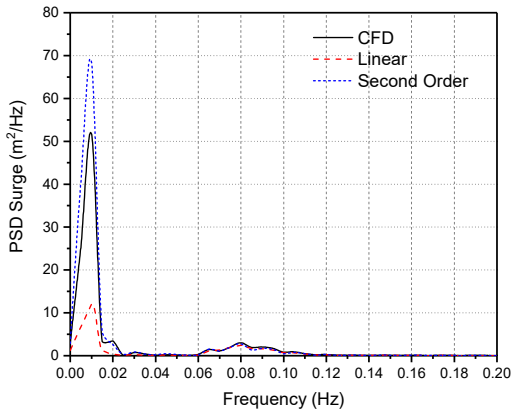

To further compare the hydrodynamics responses between CFD and potential theory approach, the Power Spectral Density comparisons are presented in Figure 13. The sampled data are selected between t=0s to t=200s.

It is obvious that both CFD and EDF results are able to capture the responses in the wave energy ranging from 0.06Hz to 0.14Hz. As to the surge motion, the linear results under-estimated the wave loading around the surge natural frequency of 0.0093Hz due to the ignored mean drift while this is included in both CFD and second order theory. However, for the pitch response, both the linear and the second-order models provides lower results than the CFD model around the pitch natural frequency of 0.037Hz. As already mentioned, this could be due to the difference in the viscous forces description, or to differences in the second order loads calculation: perturbation theory for potential flow (relying on small wave height and small floater motion) ; directly computed by the CFD model using instantaneous free surface and floater position. More investigations would be necessary to fully understand the differences observed between the models. Unfortunately, no obvious large peaks can be observed in the floater motion spectra at high frequency (larger than the wave frequency range), as floater acts like a filter, which may cut high frequencies with its inertia. Another explanation is that the majority of nonlinearity associated with a semi-submersible platform dynamic motion is caused by the second-order difference frequency wave loading.

Wave parameters impact on the platform motion responses

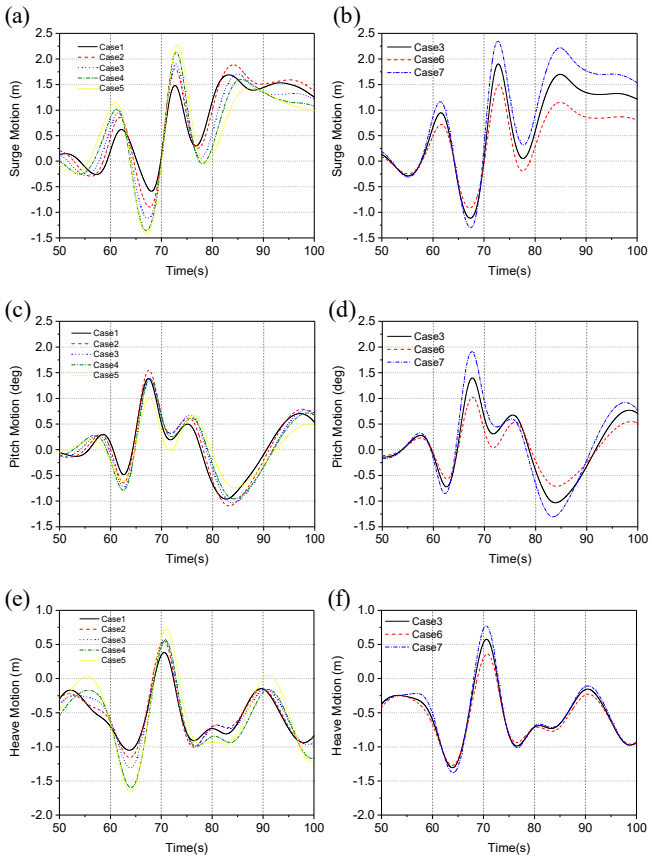

Figure 14 Surge and Pitch comparison in time series for Case1 to Case7 (a) & (b) Surge (c) & (d) Pitch (e) & (f) Heave

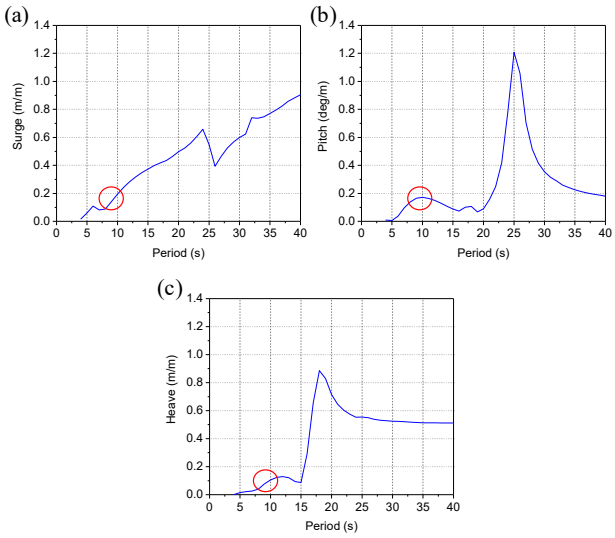

Figure 15 RAOs from EDF code for (a) surge (b) heave (c)Pitch

The platform motions under various maximum wave height H_{max} and wave period T_{Hmax} are presented in Figure 14(a) to (e) for Case 1 to 7. In general, the translational motions, i.e. the surge and heave, are influenced significantly by the variation of incident wave period and wave height. However, the pitch motions are not affected obviously under different wave periods. Given Figure 14(a) (c) (e) showing the results under different trough-to-trough period (T_{Hmax}), it is seen that the surge and heave response increase as the T_{Hmax} is ascending. Differences can be found among Case 1-5 for pitch responses but they are not very remarkable. The results are in an agreement with the Response Amplitude Operators (RAO) curves in Figure 15 from EDF results (the red circle remarks the present wave periods we are simulating and investigating). As seen, the pitch motion is nearly stable (T_{Hmax} = 8s to 10s) while the surge and heave motions increase afterwards. The results in Figure 14(b)(d)(f) also show that the surge, heave and pitch responses become large as the wave height goes up.

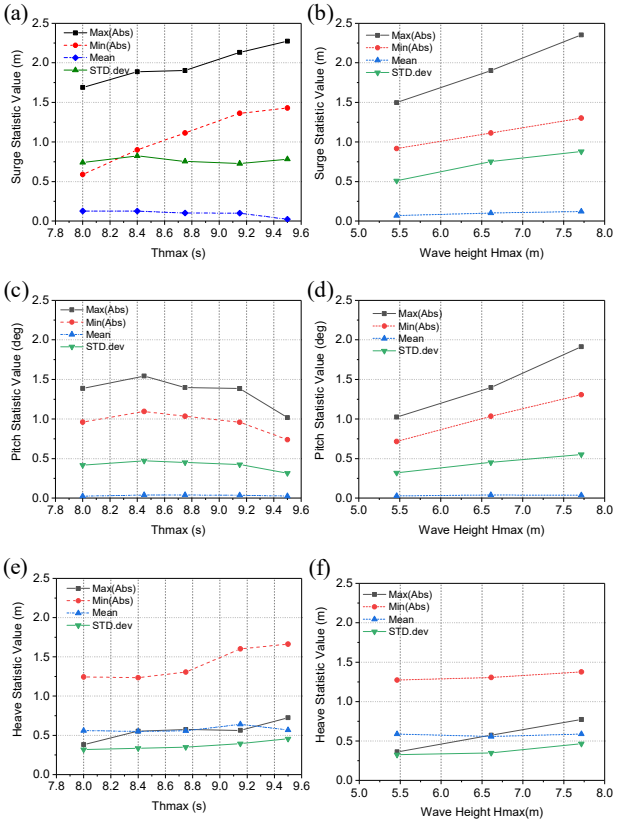

Figure 16 Statistic results of Case 1 to Case 7(a) & (b) Surge (c) & (d) Pitch (e) & (f) Heave

The statistical analysis is commonly used to analyse the data for irregular waves studies [15]. As such, we adopt this methodology for our time-domain data analysis. The statistic results given in Figure 16 are estimated within a time window of t=0s to 200s, about 100,000 sampling data are used. The Max(Abs) and Min(Abs) represent the absolute maximum and minimum platform responses while the mean and STD.dev represent the average value and the standard deviation accordingly.

As seen from Figure 16(a)(c)(e), the surge and heave responses increase as the T_{Hmax} goes up, because the T_{Hmax} becomes closer to surge and heave natural frequency of structure. However, no obvious ascending or descending trend is found for pitch motion. The time-mean values and the standard deviation remain in a similar manner for all five cases

Moving to the results under different maximum wave height, listed in Figure 16(b)(d)(f), the maximum, minimum and STD.dev value increase as the maximum wave height goes up. The mean values does not change.

Conclusion

This paper investigated a DeepCwind semi-submersible platform's dynamics response under focused wave conditions. It started with the verification of numerical wave generation for a focused wave followed by a study on a fixed FPSO platform. It was then extended to the examinations on the influence of wave parameters on the hydrodynamic response of the OC4 platform. The comparison between the CFD predictions and the date from a potential flow approach (linear theory and second order theory) indicated a good agreement between two results for PSD results near wave energy range. However, the discrepancy are observed within the natural frequency range. This could be due to the different strategies used for second order loads and viscous effects calculation. The results from varying focused wave parameters study indicated that the platform translational motions, like surge and heave, increase as the wave period is rising. However, the pitch motion is not affected too much. The CFD results are consistent with the RAO curve predicted by EDF. Due to the limited cases simulated in the present study, although the nonlinear results was observed in the CFD results, the strong nonlinearity, which often occurs at extremely large wave amplitude was not captured with the parameters selected, which requires further investigation in the near future.

Acknowledgement

Results were obtained using the Cirrus UK National Tier-2 HPC Service at EPCC (http://www.cirrus.ac.uk) funded by the University of Edinburgh and EPSRC (EP/P020267/1). The first author would like to thank China Scholarship Council (CSC) for the financial support during his PhD study in the UK.

Reference:

[1] WindEurope, 2018, "Wind in power 2017," European statistics, p. 11.
[2] Kang, J., Sun, L., and Guedes Soares, C., 2018, "Fault Tree Analysis of floating offshore wind turbines," Renewable Energy.
[3] Tran, T. T., and Kim, D.-H., 2016, "Fully coupled aero-hydrodynamic analysis of a semi-submersible FOWT using a dynamic fluid body interaction approach," Renewable Energy, 92, pp. 244-261.
[4] Liu, Y., Xiao, Q., Incecik, A., Peyrard, C., and Wan, D., 2017, "Establishing a fully coupled CFD analysis tool for floating offshore wind turbines," Renewable Energy, 112, pp. 280-301.
[5] Nematbakhsh, A., Olinger, D., and Tryggvason, G., 2014, Nonlinear simulation of a spar buoy floating wind turbine under extreme ocean conditions.
[6] Baldock, T., Swan, C., and Taylor, P., 1996, "A laboratory study of nonlinear surface waves on water," Phil. Trans. R. Soc. Lond. A, 354(1707), pp. 649-676.
[7] Gao, N., Yang, J., Tian, X., and Li, X., 2016, "A numerical study on the nonlinear effects in focused wave modelling and forces on a semi-submerged horizontal cylinder," Ships and Offshore Structures, 12(4), pp. 474-485.
[8] Mai, T., Greaves, D., Raby, A., and Taylor, P. H., 2016, "Physical modelling of wave scattering around fixed FPSO-shaped bodies," Applied Ocean Research, 61, pp. 115-129.
[9] Jacobsen, N. G., Fuhrman, D.R., Fredse,J., 2012, "A wave generation toolbox for the open-source libradry: OpenFOAM," Internationa Journal Numerical Methods in Fluid, 70, pp. 1073-1088.
[10] OpenFOAM, 2018, "The OpenFOAM Foundation Website."
[11] Hirt, C. W., and Nichols, B. D., 1981, "Volume of fluid (VOF) method for the dynamics of free boundaries," Journal of computational physics, 39(1), pp. 201-225.
[12] Hasselmann, K., Barnett, T., Bouws, E., Carlson, H., Cartwright, D., Enke, K., Ewing, J., Gienapp, H., Hasselmann, D., and Kruseman, P., 1973, "Measurements of wind-wave growth and swell decay during the Joint North Sea Wave Project (JONSWAP)," Ergänzungsheft 8-12.
[13] Li, Q., Zhuang, Y., Wan, D., and Chen, G., 2018, "Numerical Analysis of the Interaction Between a Fixed FPSO Benchmark Model and Focused Waves," The 28th International Ocean and Polar Engineering Conference, International Society of Offshore and Polar Engineers, Sapporo, Japan, p. 8.
[14] Jonkman, J., Butterfield, S., Musial, W., and Scott, G., 2009, "Definition of a 5-MW reference wind turbine for offshore system development."
[15] Coulling, A. J., Goupee, A. J., Robertson, A. N., Jonkman, J. M., and Dagher, H. J., 2013, "Validation of a FAST semi-submersible floating wind turbine numerical model with DeepCwind test data," Journal of Renewable and Sustainable Energy, 5(2), p. 023116.
[16] Finnegan, W., and Goggins, J., 2012, "Numerical simulation of linear water waves and wave–structure interaction," Ocean Engineering, 43, pp. 23-31.
[17] Antonutti, R., Peyrard, C., Johanning, L., Incecik, A., and Ingram, D., 2016, "The effects of wind-induced inclination on the dynamics of semi-submersible floating wind turbines in the time domain," Renewable Energy, 88, pp. 83-94.
[18] Antonutti, R., Peyrard, C., Incecik, A., Ingram, D., and Johanning, L., 2018, "Dynamic mooring simulation with Code_Aster with application to a floating wind turbine," Ocean Engineering, 151, pp. 366-377.
[19] Babarit, A., and Delhommeau, G., "Theoretical and numerical aspects of the open source BEM solver NEMOH,"

Proc. 11th European Wave and Tidal Energy Conference (EWTEC2015).
[20] Cummins, W. E., David, W. T. M. B., and Symposium on Ship, T., 1962, The impulse response function and ship motions, Dept. of the Navy, David Taylor Model Basin, [Washington, D.C.].
[21] Shin, H., Kim, B., Dam, P. T., and Jung, K., "Motion of OC4 5MW semi-Submersible offshore wind turbine in irregular waves," Proc. ASME 2013 32nd International Conference on Ocean, Offshore and Arctic Engineering, OMAE 2013, June 9, 2013 - June 14, 2013, American Society of Mechanical Engineers, pp. Ocean, Offshore and Arctic Engineering Division.